

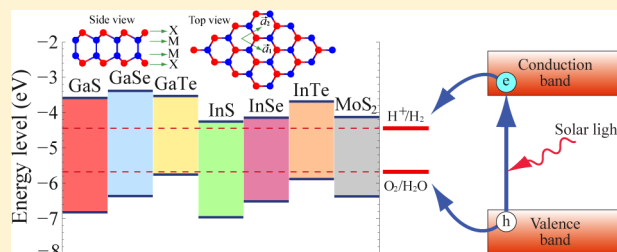
Single-Layer Group-III Monochalcogenide Photocatalysts for Water Splitting

Houlong L. Zhuang and Richard G. Hennig*

Department of Materials Science and Engineering, Cornell University, Ithaca, New York 14853, United States

ABSTRACT: The recent synthesis of single-layer GaS and GaSe opens the question of stability for other single-layer group-III monochalcogenides (MX, M = Ga and In, X = S, Se, and Te) and how the dimension reduction affects the properties of these materials. Using a first-principles design approach, we determine that the single-layer group-III monochalcogenides exhibit low formation energies and are suitable for photocatalytic water splitting. First, density-functional calculations using a van der Waals functional reveal that the monochalcogenides have formation energies similar to that of single-layer MoS₂, implying the ease of mechanically extracting single-layer monochalcogenides from their layered bulk counterparts. Next, calculations using a hybrid density functional and the quasiparticle many-body G_0W_0 approximation determine the conduction and valence band edge positions. Comparing the band edge positions with the redox potentials of water shows that single-layer monochalcogenides are potential photocatalysts for water splitting. Moreover, the bandgaps, band edge positions, and optical absorption of the single-layer monochalcogenides can be tuned by biaxial strain to increase the efficiency of solar energy conversion. Finally, calculations of the enthalpy of solvation of the single-layer monochalcogenides suggest their stability in aqueous solution.

KEYWORDS: monolayers, photocatalysis, semiconductors, nanostructures



1. INTRODUCTION

Group-III monochalcogenides (MX, M = Ga and In, X = S, Se, and Te) have been extensively studied due to their potential applications in fields such as solar energy conversion.^{1,2} For example, solar cells based on InSe have achieved efficiencies as high as 10.9%.¹ The ultimate dimension reduction of three-dimensional MX leads to single-layer MX, which consist of four sublayers stacked in the sequence X–M–M–X, as illustrated in Figure 1a. Experimental efforts have recently been undertaken to fabricate these MX in single-layer form, and single-layer GaS and GaSe sheets have already successfully been synthesized.^{3–5}

The reduction of a materials' dimension from 3D to 2D frequently results in novel electronic and mechanical properties. An example for electronic properties is given by recent experimental studies that have shown that single-layer MoS₂

exhibits a wider bandgap than its 3D bulk counterpart.^{6,7} For mechanical properties, 2D materials are often easier to strain. For instance, pristine graphene can withstand strains of up to 25%,⁸ which is significantly larger than that of graphite with a maximum elastic strain of 0.1%.⁹ In view of these unusual 2D properties, it is desirable to determine the potential of single-layer MX materials for solar energy conversion and photocatalysis.

Hydrogen generation by photocatalytic water splitting presents a promising method for solar energy conversion.¹⁰ Figure 1b illustrates the working principle of water splitting.¹¹ When sun light shines on a semiconductor, the photons can generate pairs of electrons and holes. The excited electrons can then take part in the hydrogen reduction reaction generating H₂: $2\text{H}^+ + 2\text{e}^- \rightarrow \text{H}_2$. The holes, on the other hand, participate in the oxidation reaction to generate O₂: $\text{H}_2\text{O} + 2\text{h}^+ \rightarrow \frac{1}{2}\text{O}_2 + 2\text{H}^+$. In order for a semiconductor to facilitate photocatalytic water-splitting, two conditions need to be satisfied. First, the bandgap of the semiconductor must exceed the free energy of water splitting of 1.23 eV.¹² Second, a suitable photocatalyst material requires that its conduction band minimum (CBM) energy is higher than the reduction potential of H⁺/H₂ and its valence band maximum (VBM) energy lower than the oxidation potential of O₂/H₂O.

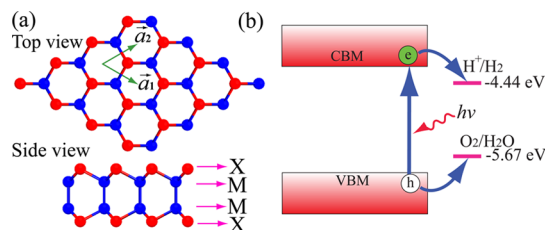


Figure 1. (a) Top and side views of the single-layer MX structure. (b) Illustration of photocatalytic water splitting. The band edge positions of a photocatalyst must be aligned with reference to the redox potentials for water splitting.

Received: May 22, 2013

Revised: June 28, 2013

Published: July 2, 2013



Table 1. Structural Parameters and Elastic Modulus of Single-Layer MX and MoS₂ Calculated with the PBE and HSE06 Functionals^a

	a_0^{PBE}	a_0^{HSE06}	$b_{\text{M-M}}^{\text{PBE}}$	$b_{\text{M-M}}^{\text{HSE06}}$	$b_{\text{M-X}}^{\text{PBE}}$	$b_{\text{M-X}}^{\text{HSE06}}$	$\theta_{\text{X-M-M}}^{\text{PBE}}$	$\theta_{\text{X-M-M}}^{\text{HSE06}}$	C^{PBE}	C^{HSE06}
GaS	3.64	3.58	2.48	2.45	2.37	2.33	117.49	117.47	98	120
GaSe	3.82	3.75	2.47	2.44	2.50	2.46	118.12	118.17	79	104
GaTe	4.14	4.06	2.47	2.44	2.71	2.66	118.14	118.21	66	84
InS	3.94	3.88	2.82	2.78	2.57	2.53	117.61	117.68	73	89
InSe	4.09	4.02	2.82	2.77	2.69	2.65	118.54	118.60	60	76
InTe	4.39	4.31	2.81	2.77	2.89	2.84	118.81	118.91	39	63
	a_0^{PBE}	a_0^{HSE06}	$b_{\text{Mo-S}}^{\text{PBE}}$	$b_{\text{Mo-S}}^{\text{HSE06}}$	$b_{\text{S-S}}^{\text{PBE}}$	$b_{\text{S-S}}^{\text{HSE06}}$	$\theta_{\text{S-Mo-S}}^{\text{PBE}}$	$\theta_{\text{S-Mo-S}}^{\text{HSE06}}$	C^{PBE}	C^{HSE06}
MoS ₂	3.18	3.15	2.41	2.39	3.13	3.11	80.80	81.02	165	189

^aThe parameters include the lattice parameter a_0 , the M–M bond length $b_{\text{M-M}}$, M–X bond length $b_{\text{M-X}}$ in units of Å, and the X–M–M bond angle $\theta_{\text{X-M-M}}$ in units of degrees. The elastic modulus C is in units of N/m.

In addition to fulfilling the above criteria on their electronic structure, the 2D MX studied in this work exhibit another advantage for applications as photocatalysts. The 2D nature of these materials means that they maximize their surface area available for water splitting while at the same time minimizing the distance that the generated electrons and holes have to migrate, reducing the possibility of electron–hole recombination and potentially enhancing their catalytic performance.¹¹

This work focuses on the exploration of single-layer MX as photocatalysts for water splitting to generate hydrogen. We first determine the stability of the materials, followed by the study of the electronic structures of single-layer MX using accurate hybrid density functional and many-body quasiparticle calculations. Next, we study how mechanical strains can be used to tune the bandgap, band edge positions, and optical absorption of the MX to increase the potential efficiency of solar energy conversion. Finally, we address the question of stability of single-layer monochalcogenides in aqueous solution by calculating the enthalpy of solvation and comparing the results to related materials with known solubility.

2. METHODS

We perform density-functional theory (DFT) calculations using the projector augmented wave method as implemented in the plane-wave code VASP.^{13–15} For the structural relaxations we employ both the PBE generalized gradient approximation (GGA) and the Heyd–Scuseria–Ernzerhof (HSE06) hybrid functional.^{16,17} A cutoff energy of 400 eV for the plane wave basis set is used throughout all calculations and ensures an accuracy of the energy of 1 meV/atom. The k -point sampling uses the Monkhorst–Pack scheme¹⁸ and employs for the single-layer materials a $48 \times 48 \times 1$ mesh for the PBE functional and an $18 \times 18 \times 1$ mesh for the more expensive HSE06 and G_0W_0 calculations. For the single-layer materials a vacuum spacing of 18 Å ensures that the interactions between the layers are negligible.

We define the formation energy E_f of the single-layer MX as

$$E_f = E_{2D}/N_{2D} - E_{3D}/N_{3D} \quad (1)$$

where E_{2D} and E_{3D} are the energies of the single-layer and bulk MX, respectively. N_{2D} and N_{3D} denote the numbers of atoms in the respective unit cells. The single-layer MX exhibits hexagonal structures with space group $P\bar{6}m2$ as illustrated in Figure 1. The 3D bulk structures of GaS, GaSe, GaTe, and InSe possess the same structure with space group $P6_3/mmc$, while InS and InTe have structures with space groups $Pnnm$ and $I4/mcm$, respectively.¹⁹ To accurately account for dispersion interactions, we use the vdW-optB88 van der Waals functional for the calculation of the formation energies.²⁰

We determine the band edge positions E_{CBM} and E_{VBM} relative to the vacuum level using the HSE06 and the G_0W_0 method by aligning the energy levels for the different materials such that their vacuum levels are set to zero. For the G_0W_0 method we follow the method by

Toroker et al.²¹ and determine the CBM and VBM levels from the bandgap center energy E_{BGC} of the HSE06 functional and the quasiparticle bandgap energy E_g^{QP} as

$$E_{\text{CBM/VBM}}^{\text{QP}} = E_{\text{BGC}}^{\text{HSE06}} \pm \frac{1}{2} E_g^{\text{QP}} \quad (2)$$

The validity of this approach relies on the assumption that, in contrast to the bandgaps, the band gap center energies are insensitive to the choice of exchange–correlation functional. As shown below, the band gap center energies of the PBE and HSE06 functional for the MX differ by merely 0.01–0.14 eV, verifying this assumption. Further details about the calculation of the bandgap center energies are given in the Appendix. We use the PBE wave functions as the starting point for the G_0W_0 calculations. Moreover, we use 64 bands and 96 frequency points, ensuring that the quasiparticle bandgaps E_g^{QP} are converged to 1 meV.

For the water splitting reaction, the redox potentials depend on the pH value.²² Here, we adopt the commonly used value of $E_{\text{H}^+/\text{H}_2}^{\text{red}} = -4.44 \text{ eV} + \text{pH} \cdot 0.059 \text{ eV}$ for the standard reduction potential for H^+/H_2 .^{22–24} Correspondingly, the oxidation potential for $\text{O}_2/\text{H}_2\text{O}$ is $E_{\text{O}_2/\text{H}_2\text{O}}^{\text{ox}} = -5.67 \text{ eV} + \text{pH} \cdot 0.059 \text{ eV}$.

To evaluate the optical properties of single-layer MX, we calculate the optical absorbance $A(\omega)$ given by $A(\omega) = \epsilon_2 L \omega / c$, where ϵ_2 is the imaginary permittivity calculated within the independent particle approximation, L is the vacuum spacing of 18 Å between the isolated MX layers, and c is the speed of light in vacuum.²⁵ Accurate calculations of the imaginary permittivity ϵ_2 require a dense k -point mesh. We use the PBE functional and a $300 \times 300 \times 1$ k -point mesh for the calculations.

To determine how easy the MX can be strained and how strain affects the electronic and optical properties we perform DFT calculations applying a biaxial strain ϵ to the materials. We calculate the elastic modulus C , an important measurable property of single-layer materials such as graphene and MoS₂,^{26,27} using

$$C = \frac{1}{A_0} \frac{\partial^2 E}{\partial \epsilon^2} \quad (3)$$

where A_0 is the equilibrium area of the simulation cell and E is the energy at strain ϵ .

3. RESULTS

3.1. Structural Properties. Table 1 reports the structural parameters of the single-layer MX calculated with both the PBE and HSE06 functionals. Our calculated structural parameters agree well with previous studies of GaS and MoS₂.^{28,29} The comparison of PBE and HSE06 lattice parameters reveals an interesting trend that the latter results are smaller than the former ones. The HSE06 functional includes 25% of exact exchange for short distances, which reduces the self-interaction

error in the PBE functional and improves the agreement with experimental lattice parameters.³⁰

Figure 2 shows that the formation energies of the single-layer MX materials are comparable or only slightly larger than the

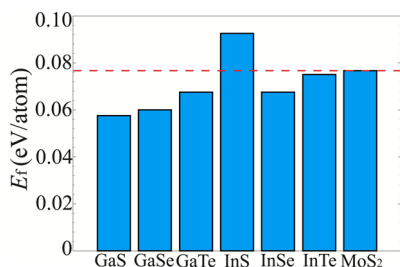


Figure 2. Formation energies of single-layer MX and MoS₂. The low formation energies indicate that the MX, similar to MoS₂, could be synthesized by mechanical exfoliation.

formation energy of single-layer MoS₂, which has been successfully synthesized by micromechanical exfoliation.³¹ Therefore, we expect that the single-layer MX can also be easily synthesized by cleaving their 3D counterparts. Indeed single-layer GaS and GaSe have already successfully been synthesized.^{3–5}

Table 1 shows the elastic moduli of single-layer MX and MoS₂ calculated with the PBE and HSE06 functionals. The elastic moduli of the MX are significantly smaller than that of MoS₂, implying that single-layer MX are softer and can be more easily strained than MoS₂. Moreover, the moduli decrease in the Ga and In monochalcogenides when the chalcogen atoms vary from S to Te. The same trend of elastic modulus is observed in the families of molybdenum and tungsten dichalcogenides.³² Although no experimental elastic moduli are available for MX, our calculated values for MoS₂ are in excellent agreement with the experimental result,²⁶ indicating the accuracy of DFT for these single-layer materials.

Interestingly, the elastic moduli from HSE06 are systematically larger than the ones from PBE. Notably, the elastic modulus of single-layer MoS₂ of 189 N/m obtained from the HSE06 functional is in excellent agreement with the experimental mean value of 180 N/m.²⁶ Similar to the difference between LDA and GGA functionals, the larger elastic moduli are likely due to the smaller lattice parameters predicted by the HSE06 functional.³⁰

3.2. Electronic Properties. Figure 3 shows the band structures of single-layer MX obtained from the HSE06 functional. As can be seen, all the MX materials display indirect bandgaps with the VBM located between the Γ and M points. The CBM for these materials, however, occurs at two different positions. For GaS and GaTe, the CBM is at the M point, while for the other four materials it is at the Γ point. For most MX, the direct bandgaps are close in size and position to the indirect bandgaps with a maximum energy difference of 0.1 eV. We expect that the direct interband transitions at the Γ point improve the optical absorption of these materials, since no phonons are required for this optical transition to proceed.

To understand the bonding characteristics of single-layer MX, we analyze their total and projected density of states, TDOS and PDOS, respectively. Figure 4a shows that the TDOS of GaSe exhibits multiple van Hove singularities over the entire energy range, which is consistent with the 2D nature of a single-layer material.³³ The corresponding PDOS of GaSe

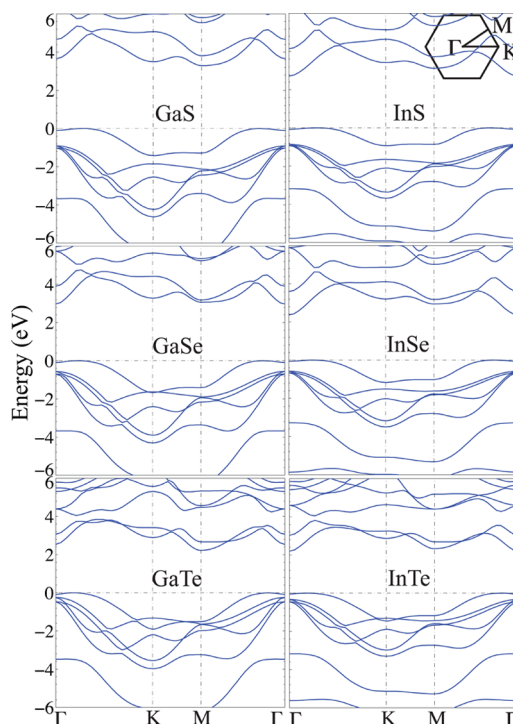


Figure 3. Band structures of single-layer MX calculated with the HSE06 functional. The valence band maximum is set to zero. The inset illustrates the first Brillouin zone of the single-layer hexagonal MX structures.

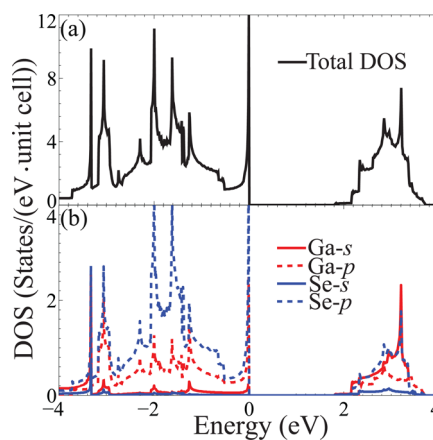


Figure 4. (a) Total and (b) projected density of states of GaSe.

in Figure 4b illustrates that the valence band of GaSe is dominated by Ga and Se 4p states, indicating hybridization between those orbitals and a covalent band character, which is typical for layered metal chalcogenides.³⁴

Table 2 summarizes the bandgaps of single-layer MX and MoS₂ calculated with the PBE and HSE06 functionals and the G_0W_0 method. With all three methods, we observe a decrease in the bandgaps for both the Ga and In monochalcogenide families as the chalcogen species changes from S to Te, which is due to the decrease in ionicity.³⁵ The PBE functional as usual underestimates the bandgaps³⁶ and predicts gaps 0.6–1.4 eV smaller than the HSE06 functional and the G_0W_0 approximation. The HSE06 and G_0W_0 methods predict similar bandgaps with the G_0W_0 bandgaps being about 0.4 to 0.6 eV larger. There is no experimental bandgap data for single-layer MX. However, our HSE06 and quasiparticle bandgaps of MoS₂

Table 2. Bandgaps E_g , Bandgap Centers E_{BGC} , and Band Edge Positions E_{VBM} and E_{CBM} of Single-Layer MX Obtained from Different Methods^a

	E_g^{PBE}	E_g^{HSE06}	E_g^{QP}	E_{BGC}^{PBE}	E_{BGC}^{HSE06}	E_{CBM}^{HSE06}	E_{CBM}^{QP}	E_{VBM}^{HSE06}	E_{VBM}^{QP}
GaS	2.48	3.19	3.82	−5.07	−5.17	−3.58	−3.26	−6.77	−7.08
GaSe	1.91	2.98	3.34	−4.92	−4.87	−3.38	−3.20	−6.36	−6.54
GaTe	1.66	2.22	2.84	−4.52	−4.64	−3.53	−3.22	−5.75	−6.06
InS	1.74	2.71	3.16	−5.55	−5.60	−4.25	−4.02	−6.96	−7.18
InSe	1.49	2.37	2.83	−5.30	−5.32	−4.14	−3.91	−6.51	−6.74
InTe	1.40	2.20	2.69	−4.79	−4.78	−3.68	−3.44	−5.88	−6.13
MoS ₂	1.68	2.25	2.36	−5.10	−5.24	−4.12	−4.06	−6.37	−6.42

^aAll energies are in units of eV. Data of single-layer MoS₂ are shown for comparison.

agree well with previous experimental and theoretical studies, indicating the accuracy of these methods.^{6,29,37} Comparison with experimental data for the single-layer materials BN, fluorographene, and MoS₂ show that the GW method in these related systems overestimates the bandgap.²⁹ The HSE06 bandgap, on the other hand, e.g., for single-layer BN, is close to the experimental value.^{38,39} Therefore, in the following discussions, we focus on the results for the HSE06 functional.

We observe that the HSE06 bandgaps reported in Table 2 for all MX except GaS fall within the visible spectrum. This indicates that these materials could harvest a significant fraction of solar light. To confirm whether they are suitable for water splitting, we need to determine the alignment of the CBM and VBM energies with the redox potentials of water.

3.3. Photocatalytic Water Splitting. Figure 5 compares the CBM and VBM energy levels with the redox potentials of

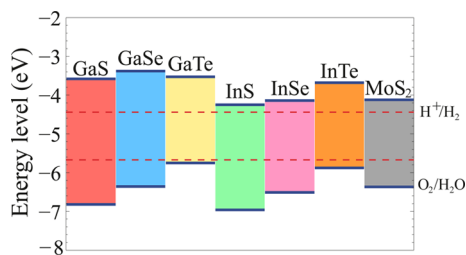


Figure 5. Band edge positions of single-layer MX relative to the vacuum level at zero strain calculated with the HSE06 functional. The band edge positions of single-layer MoS₂ and the standard redox potentials for water splitting at pH = 0 are shown for comparison.

water splitting, and Table 2 lists the values of the band edge positions relative to the vacuum level for the single-layer MX. The band edge positions of MoS₂ are shown for comparison. All the MX as well as MoS₂ have band edges located at energetically favorable positions for water splitting, suggesting that all of these seven single-layer materials are suitable photocatalysts. The same results are obtained from the G_0W_0 method, as can be seen from Table 2. Although there is no available experimental data, our prediction of single-layer MoS₂ as a potential photocatalyst is consistent with recent theoretical work.³² Note that even using the experimental bandgap of 1.9 eV for MoS₂,⁶ the resulting E_{VBM} and E_{CBM} are −4.29 and −6.19 eV, respectively. Therefore, the conclusion that single-layer MoS₂ is a suitable photocatalyst for water splitting remains the same.

The redox potentials for water increase with pH by pH·0.059 eV, shifting the water's redox energy levels in Figure 5 upward.²² This shift is beneficial to some MX, such as GaTe and InTe, since their oxidation energy levels at pH = 0 are too

close to the oxidation potential for O₂/H₂O. However, for some MX large pH values make the reduction reactions energetically unfavorable. For example, the maximum acceptable pH value for InS is 3.2.

In addition to an appropriate bandgap and a suitable band alignment, it is important that a photocatalytic material absorbs a significant fraction of the incoming light. Figure 6 shows the

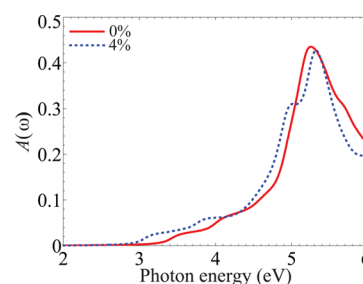


Figure 6. Optical absorbance spectrum $A(\omega)$ of single-layer GaSe at the strains of 0% and 4%. $A(\omega)$ is calculated using the PBE functional followed by a rigid energy shift to take into account the bandgap underestimation of the PBE functional.

optical absorbance $A(\omega)$ of single-layer GaSe as a function of photon energy ω . Following a previous study on TiO₂,⁴⁰ we compensate for the bandgap underestimation of the PBE functional by a rigid shift of the absorption curves upward in energy by 1.1 eV, i.e., the difference between the HSE06 and PBE bandgaps. Unlike graphene which shows a constant absorption of 2.3% in the range of visible light,²⁵ the optical absorption of GaSe increases significantly with photon energy over the range of visible light and reaches a maximum absorption of 43% at 5.2 eV. This absorption peak arises from the optical transitions between the valence and conduction bands around the *K* point. Because of the similarities in electronic structure between all the MX, we expect that the other MX exhibit a comparable optical absorption as GaSe. The high optical absorption indicates that the single-layer MX are promising candidates for photocatalytic water splitting.

3.4. Band Edge Tuning by Strain. Although all single-layer MX have suitable band edge positions with reference to the water splitting redox levels, there arise two practical concerns related to the efficiency of solar energy conversion. First, the bandgaps of some MX, e.g., GaS and GaSe, are too large to absorb a significant fraction of the solar spectrum, reducing their potential conversion efficiency. SrTiO₃, another promising photocatalyst, exhibits a similar problem of a wide bandgap of 3.2 eV, leading to efficiencies of less than 1%.⁴¹ Second, the CBM and VBM of some MX are too close to the

redox potentials of water. The CBM of InS is one such example. A useful method to address these two concerns is through bandgap engineering by applying strains.⁹ In practice, these strains could potentially be realized by epitaxial growth on suitable substrates.

To explore the effects of strain on the bandgaps and band edge positions of single-layer MX, we apply biaxial strains in the range from -4% to $+4\%$. We apply the HSE06 functional to relax atomic positions at each biaxial strain and obtain the corresponding CBM and VBM from the relaxed configurations. Figure 7 shows the variations of the CBM and VBM levels of

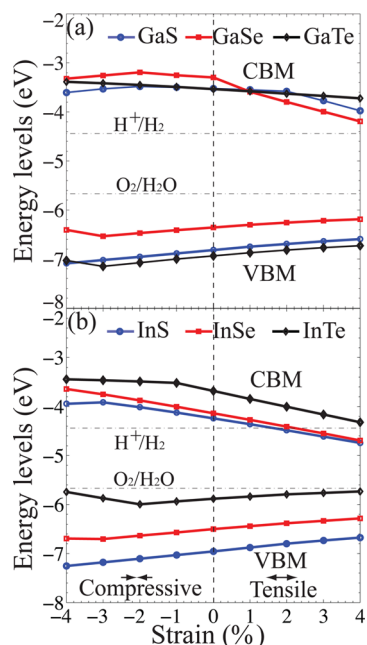


Figure 7. Strain effects on band edge positions of single-layer (a) GaX and (b) InX. Following the convention, positive strains indicate tension while negative strains denote compression. The discontinuity in slope of the band edges with strain for some MX arises from changes of the band edge positions to different k points.

the single-layer MX with strain. Over large regions of strain, the CBM and VBM level depend linearly on strain. However, for most materials we observe that the slope changes abruptly at certain strains. This is due to a change of band edge positions. For example, the CBM of GaSe at -4% strain occurs at the K point, while at $+4\%$ strain, the CBM occurs at the Γ point instead. The corresponding band structures of GaSe at these two strains are shown in the Appendix.

Transitions from an indirect to a direct bandgap and changes in the electronic structure under strain could enhance the optical absorption of the single-layer MX. Figure 6 compares the optical absorption of single-layer GaSe at zero strain and a strain of $+4\%$. The tensile strain increases the optical absorption significantly over the entire energy range of visible light.

Figure 7 provides useful guidance for tuning the bandgaps and CBM and VBM levels of single-layer MX in order to maximize the efficiency of solar energy conversion. For the GaX monochalcogenides, tensile strains are generally preferred. Tensile strains not only reduce the bandgaps but also keep both the VBM and CBM at suitable energy levels. For example, for GaS, a biaxial tensile strain of $+4\%$ reduces the bandgap to 2.62 eV, right within the visible spectrum. For InX monochalco-

nides, on the other hand, compressive strains are suggested, which increase the bandgaps slightly but more importantly make the band edge positions more favorable. In contrast, tensile strains reduce the CBM of InS and InSe below the reduction potential of H^+/H_2 making it unsuitable for water splitting at high tensile strains.

3.5. Stability in Water. To assess the stability of single-layer gallium and indium monochalcogenides in water, we estimate their solubility by calculating the enthalpy of solvation ΔH_{solv} . The enthalpy of solvation is determined as the sum of the cohesive energy and the energy change from gas atoms to hydrated ions. For the chalcogenides we also consider the possibility of ion association decreasing the enthalpy of solvation. Details are provided in the Appendix.

As a benchmark test of our method, Figure 8a compares the calculated enthalpies of solvation ΔH_{solv} of five poorly soluble

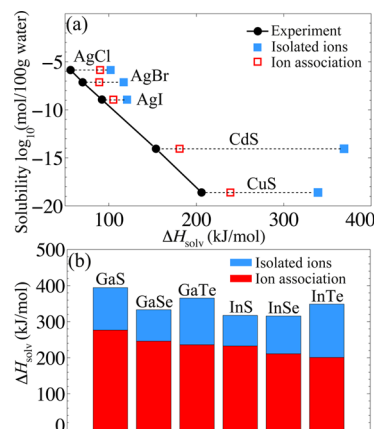


Figure 8. Stability of single-layer GaX and InX in water. (a) Experimental solubility of three silver halides and two sulfides as a function of calculated and experimental enthalpy of solvation ΔH_{solv} . (b) Predicted enthalpy of solvation ΔH_{solv} of the single-layer monochalcogenides. The high solvation enthalpies indicate that the single-layer monochalcogenides are insoluble in water.

compounds (three silver halides and two sulfides) with experimental data.^{42–44} All the experimental values are obtained from the solubility product and include an entropic term that is expected to be small. For the silver halides the calculated enthalpies correlate well with experimental data for the solubility. A similar agreement is observed for the sulfides CuS and CdS when ion association is taken into account. The difference between the experimental Gibbs energy of solvation ΔG_{solv} is nearly system independent indicating a similar entropy of solvation.

Figure 8b shows the calculated enthalpies of solvation ΔH_{solv} of the single-layer gallium and indium monochalcogenides considering either isolated ions or ion association. The solvation enthalpies are all larger than 200 kJ/mol. Comparison with the solubility of the known compounds shown in Figure 8a indicates that the solubility of the single-layer monochalcogenides are below 10^{-16} mol/100 g water, implying their stability in water.

4. CONCLUSIONS

We performed a systematic search for potential photocatalysts in the family of group-III monochalcogenides. We find that the formation energies of the single-layer MX are low and comparable to those of single-layer MoS_2 which has been

successfully synthesized. Our calculations of the bandgaps and band edge positions using accurate hybrid functional and quasiparticle methods predict that the MX are suitable photocatalysts for water splitting. We show that the MX absorb a significant amount of light in the visible range. Additionally, we show that mechanical strains can be applied to tune the bandgaps, band edge positions, and optical absorption for a better match with the solar spectrum and the redox potentials of water in order to increase the efficiency of solar energy conversion. Finally, we predict high enthalpies of solvation for the single-layer monochalcogenides, indicating that they are insoluble in water. These results provide valuable guidance for synthesis efforts of single-layer monochalcogenide materials and for their potential applications as photocatalysts.

■ APPENDIX

Method of Calculating Bandgap Center Energy

Figure 9 shows the average electrostatic potential for single-layer GaSe along the direction perpendicular to the layer

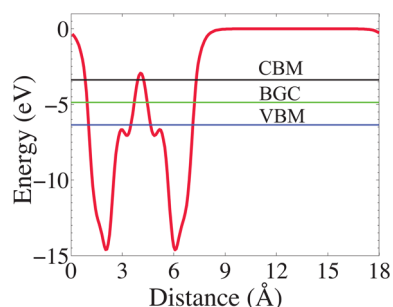


Figure 9. Average electrostatic potential (red curve) of single-layer GaSe along the direction perpendicular to the layer calculated with the HSE06 functional. The vacuum energy level is set to zero. The conduction band minimum and valence band maximum (CBM and VBM) are shown, along with the bandgap center (BGC) energy. All these three energy levels are with reference to the vacuum level.

calculated using the HSE06 functional. Shifting the energy scale, such that the vacuum level is set to zero, determines the alignment of the CBM and VBM energy levels for different materials. The bandgap center energy is given by the average of E_{CBM} and E_{VBM} .

Band Alignments of Single-Layer MX with Reference to Water's Redox Potential

Figure 10 shows the band alignments of single-layer MX and MoS_2 with reference to water's redox potential calculated using the G_0W_0 approximation to obtain the bandgaps. Similar to the HSE06 results shown in Figure 6 in the main text, the results of band alignments using the G_0W_0 bandgaps suggest that single-

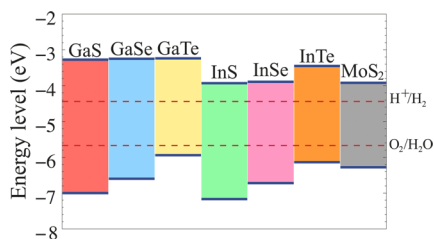


Figure 10. Band alignments of single-layer MX and MoS_2 with reference to water's redox potential calculated using the G_0W_0 approximation.

layer MX and MoS_2 are potential photocatalysts for water splitting.

Strain Effects on the Band Structure of Single-Layer GaSe

Figure 11 shows the band structures of single-layer GaSe at the strains of -4% and $+4\%$. As can be seen, at the strain of -4% ,

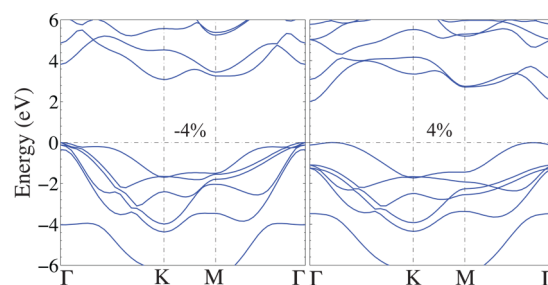
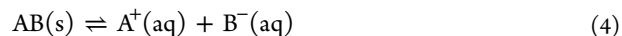


Figure 11. Band structures of single-layer GaSe at the strains of -4% and $+4\%$.

the conduction band maximum (CBM) occurs at the K point. At the strain of $+4\%$, the CBM switches to the Γ point. The change of band edge positions leads to the discontinuities in the slope of the curves shown in Figure 7 of the main text.

Enthalpy of Solvation

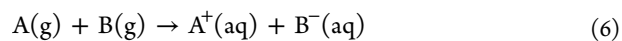
When a solid ionic compound AB(s) dissolves in water, the following solvation reaction establishes the equilibrium concentrations of the dissolved ions



Here, $\text{A}^+(\text{aq})$ and $\text{B}^-(\text{aq})$ represent A and B ions in an aqueous solution, respectively. The solubility product K_{sp} of the solvation reaction is given by the Gibbs energy of solvation ΔG_{solv} . In our following analysis, we assume that the entropy of solvation is similar for the various monochalcogenide systems and several other reference systems. To calculate the enthalpy of hydration, ΔH_{solv} , we decompose reaction 4 into two steps. First, the solid compound is separated into isolated gas atoms, i.e.,



where A(g) and B(g) are isolated A and B atoms in gas state. The enthalpy change of reaction 5, i.e. the cohesive energy of the AB compounds, ΔE_{coh} , is calculated using the PBE functional as implemented in the VASP code. In the second reaction shown below, the gas atoms are ionized and subsequently solvated in water,



To calculate the enthalpy ΔH_{hyd} of this reaction, we calculate the energy of the isolated atoms and of the hydrated ions using Gaussian09.^{45,46} The aug-cc-pVQZ basis sets are used for all calculations, and for the heavy atoms Cd, In, and Te we use effective core potentials.^{47,48} The energy of the solvated ions is calculated using several explicit water molecules and the SMD solvation model for the solute–solvent interactions.⁴⁹ We find that two water molecules are required to converge the hydration enthalpy ΔH_{hyd} to 5 kJ/mol. Ions in solution can lower their energy by forming pairs.⁵⁰ These ion associations are more likely to occur for larger cations and ions with multiple charges. We estimate the energy of associated ions by calculating the energies of cation/anion pairs solvated using the

SMD model. The enthalpy of solvation is given by the sum of the cohesive energy ΔE_{coh} and the enthalpy of hydration ΔH_{hyd} .

AUTHOR INFORMATION

Corresponding Author

*E-mail: rhennig@cornell.edu.

Notes

The authors declare no competing financial interest.

ACKNOWLEDGMENTS

We thank M. Spencer, D. Muller, F. Rana, and D. Schlom for helpful discussions. This work was supported by the NSF through the Cornell Center for Materials Research under Award No. DMR-1120296 and in part by the CAREER Award No. DMR-1056587. This research used computational resources of the Texas Advanced Computing Center under Contract No. TG-DMR050028N and of the Computation Center for Nanotechnology Innovation at Rensselaer Polytechnic Institute.

REFERENCES

- (1) Aruchamy, A. *Photoelectrochemistry and Photovoltaics of Layered Semiconductors*; Springer, 1992.
- (2) Martinez-Pastor, J.; Segura, A.; Valdes, J. L.; Chevy, A. *J. Appl. Phys.* **1987**, *62*, 1477–1483.
- (3) Hu, P.; Wang, L.; Yoon, M.; Zhang, J.; Feng, W.; Wang, X.; Wen, Z.; Idrobo, J. C.; Miyamoto, Y.; Geohagan, D. B.; Xiao, K. *Nano Lett.* **2013**, *13*, 1649–1654.
- (4) Hu, P.; Wen, Z.; Wang, L.; Tan, P.; Xiao, K. *ACS Nano* **2012**, *6*, 5988–5994.
- (5) Late, D. J.; Liu, B.; Matte, H. S. S. R.; Rao, C. N. R.; Dravid, V. P. *Adv. Funct. Mater.* **2012**, *22*, 1894–1905.
- (6) Mak, K. F.; Lee, C.; Hone, J.; Shan, J.; Heinz, T. F. *Phys. Rev. Lett.* **2010**, *105*, 136805.
- (7) Splendiani, A.; Sun, L.; Zhang, Y.; Li, T.; Kim, J.; Chim, C.-Y.; Galli, G.; Wang, F. *Nano Lett.* **2010**, *10*, 1271–1275.
- (8) Lee, C.; Wei, X.; Kysar, J. W.; Hone, J. *Science* **2008**, *321*, 385–388.
- (9) Feng, J.; Qian, X.; Huang, C.-W.; Li, J. *Nat. Photon.* **2012**, *6*, 866–872.
- (10) Grätzel, M. *Nature* **2001**, *414*, 338–344.
- (11) Kudo, A.; Miseki, Y. *Chem. Soc. Rev.* **2009**, *38*, 253–278.
- (12) Chen, S.; Wang, L.-W. *Chem. Mater.* **2012**, *24*, 3659–3666.
- (13) Kresse, G.; Furthmüller, J. *Phys. Rev. B* **1996**, *54*, 11169–11186.
- (14) Blöchl, P. E. *Phys. Rev. B* **1994**, *50*, 17953–17979.
- (15) Kresse, G.; Joubert, D. *Phys. Rev. B* **1999**, *59*, 1758–1775.
- (16) Perdew, J. P.; Burke, K.; Ernzerhof, M. *Phys. Rev. Lett.* **1996**, *77*, 3865–3868.
- (17) Heyd, J.; Scuseria, G. E.; Ernzerhof, M. *J. Chem. Phys.* **2003**, *118*, 8207.
- (18) Monkhorst, H. J.; Pack, J. D. *Phys. Rev. B* **1976**, *13*, 5188–5192.
- (19) Bergerhoff, G.; Brown, I. D. *Crystallographic Databases*; International Union of Crystallography: Chester, 1987.
- (20) Klimeš, J.; Bowler, D. R.; Michaelides, A. *Phys. Rev. B* **2011**, *83*, 195131.
- (21) Toroker, M. C.; Kanan, D. K.; Alidoust, N.; Isseroff, L. Y.; Liao, P.; Carter, E. A. *Phys. Chem. Chem. Phys.* **2011**, *13*, 16644–16654.
- (22) Chakrapani, V.; Angus, J. C.; Anderson, A. B.; Wolter, S. D.; Stoner, B. R.; Sumanasekera, G. U. *Science* **2007**, *318*, 1424–1430.
- (23) Nozik, A. J. *Annu. Rev. Phys. Chem.* **1978**, *29*, 189–222.
- (24) Jaegermann, W.; Tributsch, H. *Prog. Surf. Sci.* **1988**, *29*, 1–167.
- (25) Matthes, L.; Gori, P.; Pulci, O.; Bechstedt, F. *Phys. Rev. B* **2013**, *87*, 035438.
- (26) Bertolazzi, S.; Brivio, J.; Kis, A. *ACS Nano* **2011**, *5*, 9703–9709.
- (27) Lee, C.; Wei, X.; Kysar, J. W.; Hone, J. *Science* **2008**, *321*, 385–388.
- (28) Köhler, T.; Frauenheim, T.; Hajnal, Z.; Seifert, G. *Phys. Rev. B* **2004**, *69*, 193403.
- (29) Ataca, C.; Ciraci, S. *J. Phys. Chem. C* **2011**, *115*, 13303–13311.
- (30) Hennig, R. G.; Wadehra, A.; Driver, K. P.; Parker, W. D.; Umrigar, C. J.; Wilkins, J. W. *Phys. Rev. B* **2010**, *82*, 014101.
- (31) Novoselov, K. S.; Jiang, D.; Schedin, F.; Booth, T. J.; Khotkevich, V. V.; Morozov, S. V.; Geim, A. K. *Proc. Natl. Acad. Sci. U.S.A.* **2005**, *102*, 10451–10453.
- (32) Kang, J.; Tongay, S.; Zhou, J.; Li, J.; Wu, J. *Appl. Phys. Lett.* **2013**, *102*, 012111.
- (33) Grosso, G.; Parravicini, G. P. *Solid State Physics*; Academic: San Diego, 2000.
- (34) Wilson, J.; Yoffe, A. *Adv. Phys.* **1969**, *18*, 193–335.
- (35) Harrison, W. A. *Electronic Structure and the Properties of Solids: The Physics of the Chemical Bond*; Dover Publications: New York, 1989.
- (36) Perdew, J. P. *Int. J. Quantum Chem.* **1986**, *30*, 451–451.
- (37) Ellis, J. K.; Lucero, M. J.; Scuseria, G. E. *Appl. Phys. Lett.* **2011**, *99*, 261908.
- (38) Zhuang, H. L.; Hennig, R. G. *Appl. Phys. Lett.* **2012**, *101*, 153109.
- (39) Watanabe, K.; Taniguchi, T.; Kanda, H. *Nat. Mater.* **2004**, *3*, 404–409.
- (40) Asahi, R.; Morikawa, T.; Ohwaki, T.; Aoki, K.; Taga, Y. *Science* **2001**, *293*, 269–271.
- (41) van de Krol, R.; Liang, Y.; Schoonman, J. *J. Mater. Chem.* **2008**, *18*, 2311–2320.
- (42) Lide, D. P., Ed. *CRC Handbook of Chemistry and Physics*, 93rd ed.; CRC Press, 2012.
- (43) Dasent, W. E., Ed. *Inorganic Energetics: An Introduction*, 2nd ed.; Cambridge University Press, 1982.
- (44) Earle, Waghorne, W. *Monatshefte für Chemie/Chemical Monthly* **2003**, *134*, 655–667.
- (45) Marenich, A. V.; Cramer, C. J.; Truhlar, D. G. *J. Phys. Chem. B* **2009**, *113*, 6378–6396.
- (46) Frisch, M. J.; Trucks, G. W.; Schlegel, H. B.; Scuseria, G. E.; Robb, M. A.; Cheeseman, J. R.; Scalmani, G.; Barone, V.; Mennucci, B.; Petersson, G. A.; Nakatsuji, H.; Caricato, M.; Li, X.; Hratchian, H. P.; Izmaylov, A. F.; Bloino, J.; Zheng, G.; Sonnenberg, J. L.; Hada, M.; Ehara, M.; Toyota, K.; Fukuda, R.; Hasegawa, J.; Ishida, M.; Nakajima, T.; Honda, Y.; Kitao, O.; Nakai, H.; Vreven, T.; Montgomery, J. A., Jr.; Peralta, J. E.; Ogliaro, F.; Bearpark, M.; Heyd, J. J.; Brothers, E.; Kudin, K. N.; Staroverov, V. N.; Kobayashi, R.; Normand, J.; Raghavachari, K.; Rendell, A.; Burant, J. C.; Iyengar, S. S.; Tomasi, J.; Cossi, M.; Rega, N.; Millam, J. M.; Klene, M.; Knox, J. E.; Cross, J. B.; Bakken, V.; Adamo, C.; Jaramillo, J.; Gomperts, R.; Stratmann, R. E.; Yazyev, O.; Austin, A. J.; Cammi, R.; Pomelli, C.; Ochterski, J. W.; Martin, R. L.; Morokuma, K.; Zakrzewski, V. G.; Voth, G. A.; Salvador, P.; Dannenberg, J. J.; Dapprich, S.; Daniels, A. D.; Farkas, O.; Foresman, J. B.; Ortiz, J. V.; Cioslowski, J.; Fox, D. J. *Gaussian 09*, revision A.1; Gaussian, Inc.: Wallingford, CT, 2009.
- (47) Feller, D. *J. Comput. Chem.* **1996**, *17*, 1571–1586.
- (48) Schuchardt, K. L.; Didier, B. T.; Elsethagen, T.; Sun, L.; Gurumoorhi, V.; Chase, J.; Li, J.; Windus, T. L. *J. Chem. Inf. Model.* **2007**, *47*, 1045–1052 PMID: 17428029.
- (49) Marenich, A. V.; Cramer, C. J.; Truhlar, D. G. *J. Phys. Chem. B* **2009**, *113*, 6378–6396.
- (50) Laidler, K. J.; Meiser, J. H.; Sanctuary, B. C., Eds. *Physical Chemistry*, 4th ed.; Cengage Learning, 2002.